



# An Image Simulator of Lunar Far-Side Impact Flashes Captured from the Earth-Moon L2 Point

Da Song<sup>a,b,c</sup>, Hong-bo Cai<sup>b,\*</sup>, Shen Wang<sup>b</sup>, Jing Wang<sup>a,b</sup>

<sup>a</sup>Guangxi Key Laboratory for Relativistic Astrophysics, School of Physical Science and Technology, Guangxi University, 100 East University Road, Nanning, 530004, People's Republic of China

<sup>b</sup>Key Laboratory of Space Astronomy and Technology, National Astronomical Observatories, Chinese Academy of Sciences, A 20 Datun Road, Beijing, 100101, People's Republic of China

<sup>c</sup>School of Astronomy and Space Science, University of Chinese Academy of Sciences, Beijing, People's Republic of China

Received ---; Received in final form ---; Accepted ---;  
Available online ---

## Abstract

Impact flashes on the moon are caused by high-speed collisions of celestial bodies with the lunar surface. The study of the impacts is critical for exploring the evolutionary history and formation of the Moon, and for quantifying the risk posed by the impacts to future human activity. Although the impacts have been monitored from the Earth by a few projects in past 20 years, the events occurring on the lunar far side have not been explored systematically so far. We here present an end-to-end image simulator dedicated to detecting and monitoring the impacts from space, which is useful for future mission design. The simulator is designed for modularity and developed in the Python environment, which is mainly composed of four components: the flash temporal radiation, the background emission, the telescope and the detector used to collect and measure the radiation. Briefly speaking, with a set of input parameters, the simulator calculates the flash radiation in the context of the spherical droplet model and the background emission from the lunar surface. The resulting images are then generated by the simulator after considering a series observational effects, including the stray light, transmission of the instrument, point spread function and multiple kinds of noise caused by a CCD/CMOS detector. The simulator is validated by comparing the calculation with the observations taken on the ground. The modular design enables the simulator to be improved and enhanced by including more complex physical models in the future, and to be flexible for other future space missions.

© 2024 COSPAR. Published by Elsevier Ltd All rights reserved.

**Keywords:** Moon; Meteoroids; Impact Flash; Simulation

Email address: [chb@nao.cas.cn](mailto:chb@nao.cas.cn) (Da Song<sup>a,b,c</sup>, Hong-bo Cai<sup>b,\*</sup>, Shen Wang<sup>b</sup>, Jing Wang<sup>a,b</sup>)

<https://dx.doi.org/10.1016/j.jasr.xxxx.xx.xxx>

0273-1177/© 2024 COSPAR. Published by Elsevier Ltd All rights reserved.

## 1. Introduction

The properties and motion of small celestial bodies such as asteroids and comets are critical for understanding the evolutionary history of the solar system, because some of them are believed to contain the initial condition at the beginning of formation of the solar system (Davis et al., 2002). Unlike the meteoroids observed on Earth, which generate bright light trails due to friction with the Earth's atmosphere, the small celestial bodies can directly impact on the lunar surface at high velocity without air resistance. The impact is predicted to produce detectable optical flashes (e.g., Gordon (1921)). In addition to the properties and motion of the impactors, the study of the optical flashes enables us to explore not only the evolutionary history and formation processes of the Moon, but also the potential threats posed by meteoroids to either spacecraft or astronauts. Furthermore, lunar dust is generated by meteoroid impacts, which prompted NASA to initiate the Lunar Atmosphere and Dust Environment Explorer (LADEE) mission (Elphic et al., 2011). As part of LADEE, the Lunar Dust Experiment (LDEX) has provided new insights into the lunar dust environment and its data can also be used to estimate the flux of impactors on the lunar surface (Horanyi et al., 2015; Pokorný et al., 2019).

The optical flashes attributed to meteoroid impacts on the Moon nearside have been reported frequently by the ground-based observations in the past century. So far, hundreds of impact events have been identified. For instance, Stuart (1956) photographed a flash of light on the lunar surface likely attributed to a large meteoroid impact. As the first unequivocal detection of impact on the night side of the Moon, Ortiz et al. (2000) reported unambiguous detection of five impact flashes during the 1999 Leonid meteor shower. Three of them have been seen simultaneously by other observers (e.g., Dunham et al., 1999). Four additional flashes attributed to an impact have been reported for the Leonid meteor shower occurring in November 2001 (Ortiz et al., 2002). In addition to the Leonid meteor shower, subsequent observations have detected lunar impact flashes from the Geminid (Yanagisawa et al., 2008), Lyrid (Moser et al., 2011), Perseid (Yanagisawa et al., 2006), and Taurid meteor showers (Cooke et al., 2006), as well as sporadic impact flashes unrelated to meteor showers (Ortiz et al., 2006; Cooke et al., 2007).

In order to study lunar impact flashes systematically, Cao & Wang (2020) listed several ground-based monitoring programs focusing on the near side of the Moon that have been established since 2005, including the NASA Lunar Impact Monitoring Program (Suggs et al., 2008) initiated in 2006, the Moon Impacts Detection and Analysis System (MIDAS) program (Madiedo et al., 2010) started in 2009, and the NEO

Lunar Impacts and Optical Transients (NELIOTA) program (Bonanos et al., 2015) initiated in 2015. By using a 1.2-meter telescope equipped with a scientific camera (Andor Zyla 5.5 sCMOS) (Bonanos et al., 2018; Xilouris et al., 2018; Liakos et al., 2019), NELIOTA had confirmed 187 flash events<sup>1</sup> until July 2023.

It has still not been achieved to monitor the impact flashes occurring on the far side of the Moon. To address this, various research institutions globally have initiated studies on lunar far side impact flashes. One notable effort is the Lunar Meteoroid Impacts Observer (LUMIO) mission (Cervone et al., 2022). This CubeSat mission began its Phase 0 study in 2017, followed by an independent mission assessment by European Space Agency (ESA) in 2018. After successfully completing Phases A and B, ESA approved LUMIO to advance to Phases C and D in June 2024, which includes hardware development, with a potential launch as early as 2027. Observations of these impacts would allow us to examine the properties of lunar soil on the far side and to identify the risk caused by the impacts to future human activity on the far side.

In this paper, we develop an end-to-end image simulator for a proposed mission that monitors the lunar far side impact flashes from the Earth-Moon L2 point. With the simulated images with a set of instrumental parameters, the simulator is useful for future mission design and optimization. The paper is organized as follows. Section 2 describes the conception of the proposed mission. Based on the conception, an end-to-end image simulation is formulated in Section 3. The results of the simulation is shown in Section 4.

## 2. Mission Concept

The current image simulator is developed for a proposed mission that is described briefly as follows. By pointing to the shadow region of the Moon, a camera working simultaneously in multiple optical bands is used to monitor the far side of the Moon from the Earth-Moon L2 point that is roughly 65,000 kilometers from the Moon (Burns et al., 2013). In each band, either a CCD or a CMOS is adopted as the detector. LUMIO will operate in a quasi-halo orbit around the Earth-Moon L2 with a CCD, collecting data in the visible (VIS) and near-infrared (NIR) bands. An impact flash will be identified in real time from the obtained images by onboard dedicated pipelines based on traditional astronomical methods.

Our simulator has some similarities with the work of Merisio & Topputo (2023); Topputo et al. (2023), particularly

---

<sup>1</sup><https://neliota.astro.noa.gr/>

in simulating lunar impact flashes and evaluating camera performance using metrics like signal-to-noise ratio (SNR). However, we have further advanced these efforts. First, our simulator generates images that show the visual process of the impact flash, while their model focuses on statistical analysis based on calculations. Additionally, our model simulates how the flash dims over time until it disappears, providing a more detailed timeline for analysis. In contrast, their study uses an average flash temperature for evaluation. By expanding on this research, our simulator offers a new perspective on analyzing the time evolution of flash events.

### 3. An End-to-end Image Simulator

Based on the mission concept described above, an end-to-end image simulator is developed and specified in this section.

Figure 1 illustrates the design of the current simulator. Briefly speaking, the simulator is mainly composed of four modules: flash, background, optical system and detector. With a set of input parameters listed in Table 1, the simulator calculates the emission of a given impact flash, along with the background contributed by various sources. The emission is then translated to Analog-to-Digital Unit (ADU) counts from the detectors in the focal plane by the optical system module and detector module, which results in a final image as an output of the simulator. The details of each of the modules are described as follows.

#### 3.1. Emission from Lunar Impact Flash

We simulate the emission and evolution of an impact flash by following the model given in Yanagisawa & Kisaichi (2002). In the model, the emission of a flash can be well described by a blackbody at a temperature of  $T$

$$f_{\text{flash}}(\lambda, T) = \frac{2\pi hc^2}{\lambda^5} \cdot \frac{1}{e^{\frac{hc}{\lambda k_B T}} - 1} \quad (1)$$

where  $h, c$  and  $k_B$  are the Planck constant, the speed of light and the Boltzmann constant, respectively.

With the blackbody emission, we calculate the flux of an impact flash within a wavelength range from  $\lambda_1$  to  $\lambda_2$  by an integration

$$F(t) = \int_{\lambda_1}^{\lambda_2} \frac{f_{\text{flash}}(\lambda, T(t)) \cdot S_e}{f\pi R^2} d\lambda \quad (2)$$

where  $S_e$  is the effective area of the flash,  $f = 4$  since we adopt the molten droplet model, which is assumed to be standard spherical radiation, and  $R$  the distance to an observer.

#### 3.1.1. Flash Cooling

By following the model in Yanagisawa & Kisaichi (2002), the thermal evolution of the molten droplet can be described by the heat conduction equation:

$$\frac{\partial T}{\partial t} = \frac{\kappa}{r^2} \frac{\partial}{\partial r} \left( r^2 \frac{\partial T}{\partial r} \right) \quad (3)$$

with a radiative boundary condition at the surface with a temperature of  $T_s$ :

$$k \frac{\partial T}{\partial r} = -\sigma T_s^4 \quad (4)$$

where  $\sigma$  is the Stefan–Boltzmann constant,  $\kappa$  is the thermal diffusivity given by  $\kappa = k/(c_p \rho)$ ,  $k$  the thermal conductivity,  $\rho$  the density of the droplet, and  $c_p$  the specific heat.

The cooling model is involved in our simulator in a simplified way by assuming a uniform temperature with the droplet. This approximation is reasonable because the thermal conduction is usually faster than the radiation process (e.g., Bouley et al., 2012). In this scenario, the cooling of the droplet can be approximated by the equation integrated over volume:

$$\frac{4}{3} \pi R_d^3 \rho c_p \frac{dT}{dt} = -4\pi R_d^2 \sigma T^4 \quad (5)$$

where  $R_d$  is the droplet radius being typically on the order of tens to hundreds of micrometers (McKay et al., 1991). This equation has an analytical solution:

$$T(t) = \frac{T_0}{\left(1 + \frac{9t\sigma T_0^3}{\rho R_d c_p}\right)^{\frac{1}{3}}} \quad (6)$$

where  $T_0$  is the peak temperature. The typical value of  $c_p = 1.3 \text{ J} \cdot \text{g}^{-1} \text{K}^{-1}$  (i.e., solid glass) is adopted in the simulator for the droplet (Cintala, 1992).

#### 3.1.2. Flash Effective Area

According to the spherical droplet model proposed by Yanagisawa & Kisaichi (2002), the effective area of the flash ( $S_e$ ) can be estimated from the liquid volume  $V$

$$S_e = \frac{V}{\frac{4}{3}\pi R_d^3} \cdot 4\pi R_d^2 = \frac{3V}{R_d} \quad (7)$$

The volume  $V$  is related with the mass ( $m$ ), density ( $m_\rho$ ), and impact velocity ( $v$ ) of the meteoroid as

$$V = \frac{m}{m_\rho} (c_1 + c_2 v + c_3 v^2) \quad (8)$$

where  $c_1, c_2$  and  $c_3$  are constants depending on the meteoroid density and lunar regolith temperature, as detailed in Cintala (1992). In the simulations below, these constants are as follows: for the molten droplet model,  $c_1 = -12.1$ ,  $c_2 = 1.69$ , and  $c_3 = 0.0233$ ; for the vapor model,  $c_1 = -0.657$ ,  $c_2 = -0.107$ , and  $c_3 = 0.0211$ .

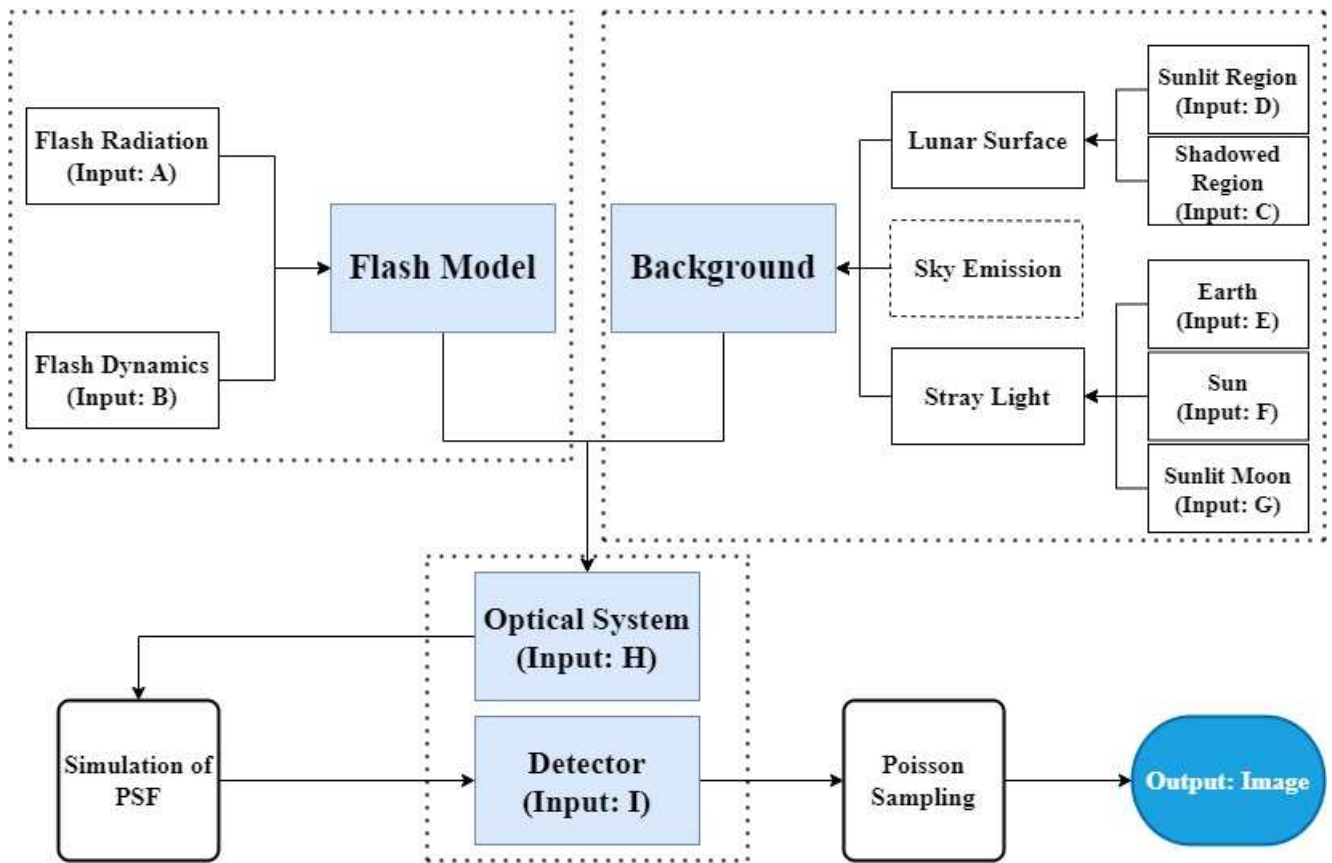


Fig. 1. Flow diagram of the flash image simulator developed by us. There are four modules in the simulator, i.e., the flash model, background, optical system and detector. In the background module, the sky emission is not included in the current version, although an interface is reserved.

Table 1. The list of the input parameters required for the simulator.

Parameters	Unit	Description
Group A		
$T_0$	K	Peak temperature of the flash
Group B		
$m$	g	Mass of meteoroid
$m_\rho$	$\text{g cm}^{-3}$	Density of meteoroid
$v$	$\text{km s}^{-1}$	Impact velocity of meteoroid
$R_d$	$\mu\text{m}$	Radius of individual molten droplet
Group C		
$T_{\text{shadow}}$	K	Lunar shadow temperature
$\bar{\varepsilon}$	/	Average emissivity of the lunar shadow region
Group D		
$f_\odot$	$\text{W m}^{-2}$	Solar irradiance
$\eta$	/	Average albedo of the Moon
$\mathbf{s}$	/	Direction of the solar light
Group E		
$f_\odot$	$\text{W m}^{-2}$	Solar irradiance
$\eta_E$	/	Average albedo of the Earth
Group F		
$f_\odot$	$\text{W m}^{-2}$	Solar irradiance
Group G		
$f_\odot$	$\text{W m}^{-2}$	Solar irradiance
$\eta$	/	Average albedo of the Moon
Group H		
$R$	m	The distance between flash and observer
$D$	mm	Aperture
$d_f$	mm	Focal length
$\tau_t$	/	Transmittance of the optical system
$\bar{\lambda}$	m	effective wavelength
$\lambda_1$	m	upper wavelength limit
$\lambda_2$	m	lower wavelength limit
$PST$	/	Stray light suppression coefficient of the optical system
Group I		
$N$	/	The number of active pixels
$d_{\text{pix}}$	$\mu\text{m}$	Individual pixel size
$\Delta t$	seconds	Exposure time
$\eta_q$	/	Average quantum efficiency of the detector
$N_r$	$e^-$	Readout noise
$I_d$	$e^- \text{pixel}^{-1} \text{s}^{-1}$	Dark current
$G$	/	Gain

### 3.2. Background Emission

The background signal from the lunar surface is taken into account in the current simulator. The emission and reflection of the lunar surface is calculated at different phases after taking the direction of the sunlight into account. The simulated brightness of the lunar surface at different phases is illustrated in Figure 2.

#### 3.2.1. Surface emission from Shadow Region

The emission from the shadow region is simulated by its own thermal radiation, which is controlled by the surface temperature and the emissivity of the regolith. The thermal radiation per unit area within the wavelength range  $\lambda_1$  to  $\lambda_2$ , which is typically considered to be uniformly emitted over a hemispherical area from the lunar surface, is given by:

$$f_{\text{shadow}} = \int_{\lambda_1}^{\lambda_2} \frac{2\pi hc^2}{\lambda^5} \frac{1}{e^{hc/(\lambda k_B T_{\text{shadow}})} - 1} \bar{\epsilon} d\lambda \quad (9)$$

where  $T_{\text{shadow}}$  is the surface temperature of the shadowed region of the Moon, approximately 110 K (Vaniman et al., 1991), and  $\bar{\epsilon}$  is the average emissivity of the lunar regolith over the wavelength range  $\lambda_1$  to  $\lambda_2$ . While this equation assumes uniform thermal radiation emission, the received radiation is related to the observation angle. Specifically, when observing at higher angles (relative to the surface normal), less radiation is received compared to lower angles, even if the surface radiates isotropically.

#### 3.2.2. Surface reflection from Sunlit Region

We simulate the radiation signal from the sunlit region of the lunar surface by a reflection of the solar radiation in the traditional Lambert illumination model (Lambert, 1760) :

$$f_{\text{sunlit}} = \int_{\lambda_1}^{\lambda_2} f_{\odot} \cdot \eta \cdot \cos \theta d\lambda \quad (10)$$

where  $\eta$  is the albedo of the lunar surface, which is taken as 0.15 and can be referenced in Heiken et al. (1991); Muinonen et al. (2011),  $f_{\odot}$  the solar irradiance at the surface, and  $\theta$  the angle between the reverse vector of the incident light and the normal vector of the surface. Our simulation adopts the irradiance outside the Earth atmosphere given by the World Meteorological Organization Instrument and Observing Methods Committee at its eighth session<sup>2</sup>. For the  $R$ -band (550-800 nm), the solar irradiance is 377 W/m<sup>2</sup>, and for the  $I$ -band (700-950 nm), it is 271 W/m<sup>2</sup>.

### 3.3. Image

#### 3.3.1. Flash

With the flux of a given impact  $F$  estimated in Eq (2), the total number of electrons generated on the CCD within an exposure time of  $\Delta t$  can be estimated as:

$$N_s = \frac{\pi D^2 \cdot F \cdot \tau_t \cdot \eta_q \cdot \Delta t}{4E_0} \quad (11)$$

where  $E_0 = hc/\bar{\lambda}$  is the energy of a single photon with an effective wavelength of  $\bar{\lambda}$ ,  $D$  the effective aperture of the telescope.  $\tau_t$  and  $\eta_q$  are the total throughput of the optical system and the average quantum efficiency of the detector, respectively.

In our simulator, each flash is considered as a point source whose profile at the focus is described by the point spread function (PSF). In the CCD coordinate  $(x, y)$ , the PSF is specified as a 2-dimensional Gauss function:

$$G(x, y) = G_0 e^{-\frac{(x-x_0)^2}{2\sigma_x^2} - \frac{(y-y_0)^2}{2\sigma_y^2}} \quad (12)$$

where  $G_0$  is the maximum value at the center,  $\sigma_x$  and  $\sigma_y$  are the dispersion in the  $x$  and  $y$  directions, respectively.

#### 3.3.2. Background

According to the estimated background emission, the corresponding photon-generated electrons recorded by each CCD pixel is calculated as

$$\begin{aligned} N_b &= \frac{f_j \cdot \left( \frac{d_{\text{pix}}^2}{d_f^2} \cdot R^2 \right) \cdot \frac{\pi D^2}{4} \cdot \tau_t \cdot \eta_q \cdot \Delta t}{2\pi R^2 \cdot E_0} \\ &= \frac{f_j \cdot d_{\text{pix}}^2 \cdot D^2 \cdot \tau_t \cdot \eta_q \cdot \Delta t}{8d_f^2 \cdot E_0} \end{aligned} \quad (13)$$

The term  $\frac{d_{\text{pix}}^2}{d_f^2} \cdot R^2$  represents the sky area corresponding to a single pixel at a distance  $R$ .  $\frac{\pi D^2}{4}$  indicates the effective area of the telescope's aperture.  $2\pi R^2$  represents the total emission area of a hemisphere.

- $f_j$  represents the radiative flux within the shadowed or sunlit regions of the Moon.
- $d_{\text{pix}}$  denotes the size of each pixel.
- $D$  is the effective aperture of the telescope.
- $\tau_t$  and  $\eta_q$  denote the total transmission of the optical system and the average quantum efficiency of the detector, respectively.
- $\Delta t$  is the exposure time.
- $d_f$  represents the focal length of the optical system.
- $E_0$  is the energy of a single photon.

<sup>2</sup>WMO: <https://library.wmo.int/idurl/4/41712>

### 3.3.3. Stray Light

The pollution produced by stray light can reduce the signal-to-noise ratio of the target by enhancing the background level artificially.

In ground-based observations, stray light is often significantly higher near the Moon's terminator and less pronounced in regions farther away.

For space-based observations, the distribution of stray light may vary due to different environmental factors and the spacecraft's design. The spacecraft's attitude, position, and orientation can all influence stray light distribution. For example, the spacecraft's solar panels or other components might reflect light into the telescope, creating stray light. Additionally, the spacecraft might cause occlusions or shadows that affect the distribution of light pollution. These factors and design considerations represent current limitations of the simulator. Consequently, at this stage of the simulation, stray light is assumed to be uniformly distributed in the focal plane.

The number of photon-generated electrons of each pixel can be estimated as

$$N_n = \frac{\sum f_i \cdot \text{PST}_i \cdot d_{\text{pix}}^2 \cdot \eta_q \cdot \Delta t}{E_0} \quad (14)$$

where  $f_i$  is the flux of sunlight, the illuminated part of the Earth, or the illuminated part of the Moon at the entrance pupil of the telescope. Specifically, for the Sun, we use the previously mentioned  $f_{\odot}$ . For the Earth and Moon, the flux is expressed as

$$f_i = \frac{f_{\odot} \cdot S_i \cdot \eta_i}{2\pi R_i^2} \quad (15)$$

where  $\eta_e = 0.29$  is the average albedo of the Earth (Stephens et al., 2015), and  $R_i$  denotes the distances from the observation point to the Earth and the Moon, respectively. The illuminated area on one side of the Earth and Moon is given by  $S_i = 2\pi r_i^2 \cdot A$ , with  $r_i$  representing the radii of the Earth and the Moon.  $A$  represents the ratio of the illuminated area to the total area on that side (depending on the moon phase).  $E_0$  the energy of a single photon,  $\eta_q$  the quantum efficiency,  $d_{\text{pix}}$  the size of each pixel, and  $\Delta t$  the exposure time. PST (a short for point source transmittance), defined as

$$\text{PST}(\alpha) = \frac{E_d(\alpha)}{E_s(\alpha)} \quad (16)$$

is used to characterize the stray light rejection capability of the optical system. Here,  $E_d(\alpha)$  and  $E_s(\alpha)$  are the irradiance received at the focal plane and that from an off-axis point source. It is influenced by the materials and structures of optical components such as baffle. A smaller PST value indicates lower levels of stray light received by the image sensor. PST is closely related to the incident angle  $\alpha$  of the source and drops significantly with the angle.

### 3.3.4. Detector

A set of parameters is adopted in our simulator to model the performance of a perfect CCD detectors (Konnik & Welsh, 2014). In addition to  $\eta_q$  and  $d_{\text{pix}}$  used above, the parameters include the total pixel numbers  $N \times N$ , bias level, dark current, readout noise and CCD gain  $G$ .

The field-of-view is therefore inferred to be  $\Delta\Omega = (N\alpha_p)^2$ , where  $\alpha_p$  is the angular size of a single pixel in the sky:

$$\alpha_p = \frac{d_{\text{pix}}}{d_f} \cdot \frac{180}{\pi} \text{ degree} \quad (17)$$

Note that the approximation  $\frac{d_{\text{pix}}}{d_f}$  is valid only for small angular sizes.

Imperfections of the CCD, such as photo-response non-uniformity, as well as the CCD smear effect, are ignored in our current simulator, although it can be easily implemented in the simulator in the future.

### 3.3.5. Noise and Final Image

The noise generated during observations mainly consists of inherent noise and signal noise. The inherent noise originates from the detector, including readout noise and dark current noise. The signal noise is mainly caused by the quantum nature of the signal and background emission.

With the calculated electrons from the flash, background and detector, the resulting image is finally obtained by a statistical sampling in each pixel according to the traditional Poisson distribution

$$P(k) = \frac{e^{-N} N^k}{k!} \quad (18)$$

After the sampling, the final ADU of each pixel is obtained from the total electrons by a given  $G$

$$\text{ADU} = \frac{N_e}{G} \quad (19)$$

where  $N_e$  is the number of electrons generated by the incoming photons.

## 4. Results and Examples

By following the methods described in Section 3, a simulator is developed with the Python 3.9 software in the Windows 10 operating system. The packages of NumPy (Harris et al., 2020), SciPy (Virtanen et al., 2020), and Astropy (Robitaille et al., 2013) are required for running the simulator, which we will make available for download to readers on GitHub<sup>3</sup>. To generate a series of images, the simulator inputs a set of parameters describing the flash radiation, the observation equipment, and

<sup>3</sup><https://github.com/luckydog9?tab=repositories>

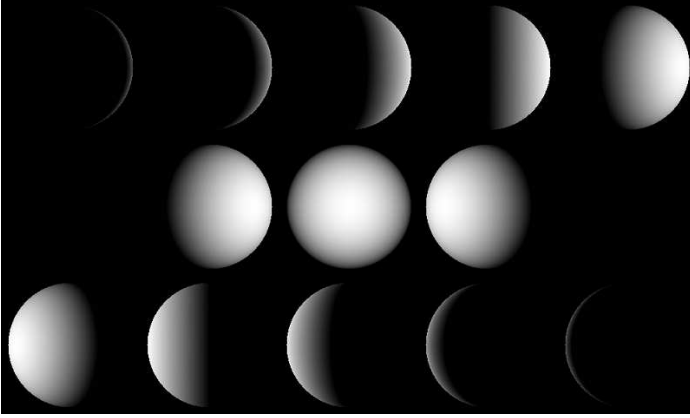


Fig. 2. The simulated lunar surface brightness at different phases. See Section 3.2 for the details.

the observation conditions, such as distance from an observer, moon phase, etc. These parameters and the simulated images are presented as follows.

#### 4.1. Definition of Flash Models

Three flash models defined by a set of typical input values are considered as an example. The used parameters are listed in Table 2.

In the droplet model given in (Cintala, 1992), the temperature ranges from 1700 K (the melting temperature of the lunar regolith) to 3800 K (the evaporation temperature). This range agrees with our statistical study on the 187 events recorded by NELIOTA. After excluding 61 events with large relative uncertainties (i.e.,  $\geq 20\%$ ), our study shows that  $\sim 85\%$  impacts have a peak temperature between 1700 and 3800 K, and the average value is  $\sim 2750$  K (see Figure 3).

Regarding the meteoroid mass, Liakos et al. (2020) estimates a rather wide range between 2.3 g and 2.7 kg from validated flash data, although the majority ( $\sim 71\%$ ) has a mass less than 100 g.

The impact velocity of meteoroids depends on their origin, which is set between  $15 \text{ km s}^{-1}$  for sporadic events (Drolshagen et al., 2020) and  $\sim 70 \text{ km s}^{-1}$  for the Leonid meteor shower. An average velocity of  $46.3 \text{ km s}^{-1}$  can be obtained from a sample of 55 meteoroids whose velocities are estimated by Avdellidou & Vaubaillon (2019).

The radius of individual small droplets produced by an impact is believed to be compared to the average grain size of lunar soil, which is approximately tens to hundreds of micrometers (McKay et al., 1991). For the density of meteoroids, we adopt the widely used assumption that meteoroids are composed of diabase with a density of  $3.0 \text{ g cm}^{-3}$  (Cintala, 1992), although the density is approximately  $1.0 \text{ g cm}^{-3}$  for common comet and is up to  $6.0 \text{ g cm}^{-3}$  for iron meteoroids.

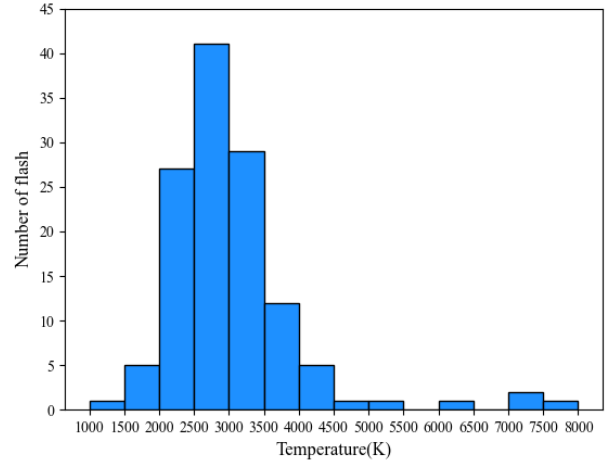


Fig. 3. Distribution of the peak temperature of the 126 flashes observed on the ground by NELIOTA, after excluding the 61 events with large relative uncertainties of the estimated temperature (i.e.,  $\geq 20\%$ ). We refer the readers to Appendix A for the details of the temperature estimation.

Table 2. The three flash models considered in the simulation.

Flash	$T_0$ (K)	$m$ (g)	$v$ (km/s)	$V$ (m <sup>3</sup> )	$r$ ( $\mu\text{m}$ )
1	1700	2.3	15	0.000014	100
2	2750	28	46.3	0.0019	80
3	3800	2700	70	0.2	50

#### 4.2. Definition of Observation Equipment

The parameters adopted to define an observation equipment is tabulated in Table 3. The corresponding field-of-view (FoV) is  $1.47^\circ \times 1.47^\circ$ . The angular diameter of the Moon as seen from the L2 point is about  $3^\circ$ , so the FoV covers about 1/4 of the Moon's surface. This FoV enables us to monitor the non-illuminated part of the Moon efficiently.

In addition, both Johnson-Cousins  $R$ - and  $I$ -bands are adopted in the subsequent image simulation.

Table 3. Optical and camera parameters considered in the simulation.

Optical system parameters		Camera parameters	
Lens aperture	200 mm	Sensor size	$7.5 \mu\text{m}$
Focal length	600 mm	Active Pixels	$2048 \times 2048$
System focal ratio	$f/3.0$	Frame frequency	30 Hz
FoV	$1.47^\circ \times 1.47^\circ$	Exposure time	23 ms
Average throughput	40%	Average quantum efficiency	90%
$\lambda_R$	641 nm	Gain	$1.0 e^-$ per A/D count
$\lambda_I$	798 nm	Read noise	$6.0 e^-$ rms
		Dark noise	$0.1 e^- \text{ pixel}^{-1} \text{ s}^{-1}$

#### 4.3. Observation Conditions

In the previous section, we introduced the definition of PST. However, determining PST requires specialized simulation software or experimental measurements. Here, we referenced the experimental results of Sholl et al. (2007), which



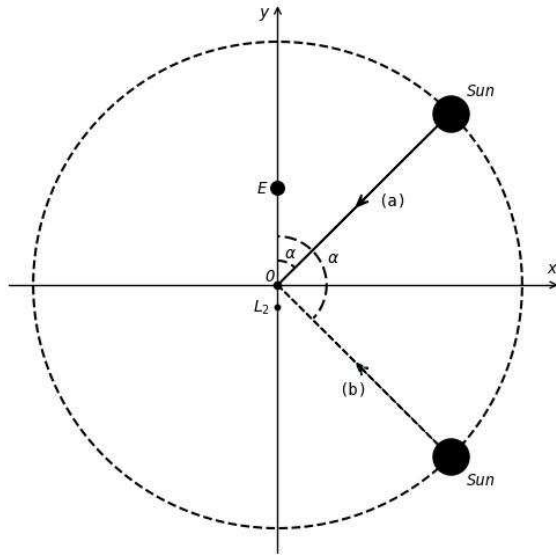


Fig. 4. An illustration of the geometry adopted in the simulator for stray light estimation. The Moon is at the center of the  $xy$  coordinate system. The Earth and the L2 point are denoted by  $E$  and  $L_2$  on the  $y$  axis. The incident radiation from the Sun at two different lunar phases is shown by the solid and dashed lines associated with an arrow. The corresponding source incident angle  $\alpha$  are marked on the plot.

demonstrate how PST changes with the angle  $\alpha$ . Based on these results, along with the geometry shown in Figure 4 and the source angle  $\alpha$ , we estimated the PST values for the Sun, Earth, and Moon at different moon phases. The estimated values we used are presented in Table 4. Although this approach is imperfect, as mentioned in Section 6, we plan to refine the PST model in our future work.

Table 4. The PST of the Sun, Earth, and Moon at different moon phases (where 0 = new Moon, 1 = full Moon).

Moon phase	PST <sub>Sun</sub>	PST <sub>Earth</sub>	PST <sub>Moon</sub>
0.1	$2 \times 10^{-5}$	$8 \times 10^{-4}$	$1 \times 10^{-2}$
0.5	$1 \times 10^{-9}$	$5 \times 10^{-3}$	$3 \times 10^{-2}$

#### 4.4. Results

With the input parameters given above and the theoretical model, the final images in the  $R$ - and  $I$ -bands at 0.1 and 0.5 moon phases are simulated for the Flash 1, 2, and 3 models listed in Table 2. Table 5 tabulates the highest signal-to-noise ratio (SNR) estimated from the simulated images in different cases. The SNR of the simulated image was calculated using the standard definition, as outlined by Raab (2002), where SNR is the signal in  $e^-$  divided by the Poisson noise in  $e^-$  RMS (Root

Mean Square). The flash intensity is measured using standard aperture photometry with a 2-pixel aperture radius, while the background intensity is assessed using annuli ranging from 6 to 14 pixels. This choice reduces contamination from the flash signal to accurately measure background intensity.

As examples, Figure 5 shows the calculated evolution of irradiance of the Flash 2 model. Then, we simulated a full-size image ( $2048 \times 2048$ ) that includes the illuminated area of the lunar surface, as shown in Figure 6. It is important to note that during actual observations, the illuminated areas should be avoided, and the field of view should be directed towards the non-illuminated part. The presence of illuminated areas within the field of view significantly reduces the efficiency of monitoring lunar impact flashes. Therefore, the NELIOTA project conducts flash observations in shadow regions when the moon phase ranges from 0.1 to 0.45 (Xilouris et al., 2018). Figure 6 is designed to help readers understand the relative intensity between the brightness of the flash and the illuminated limb of the lunar surface. The subsequent analysis focuses on simulating the temporal variations of the flash in the shadow region. By extracting the  $30 \times 30$  pixel area centered on the flash, Figure 7 and 8 illustrate the temporal variations of the simulated Flash 2 images taken at the 0.1 moon phase. Similar images taken at the 0.5 moon phase are displayed in Figure 9 and 10.

Three facts can be learned from the simulated images and the corresponding SNRs. At first, the flashes generated by meteoroid impacts tend to be more easily detected in the  $I$ -band than the  $R$ -band, which is consistent with the trend observed by NELIOTA project: the flashes detected in the  $I$ -band outnumber those detected in the  $R$ -band. Possible reasons include: 1) the lunar surface brightness in the  $I$ -band is lower than that in the  $R$ -band, resulting in weaker stray light in the  $I$ -band; 2) the radiation of the flashes is more prominent in the near-infrared.

Secondly, in a given band, the number of the flashes detected at the 0.5 moon phase is slightly higher than that at the 0.1 moon phase, which is mainly caused by a reduced stray light (i.e., a reduced PST value) at the 0.5 moon phase.

Finally, an event described by the Flash 1 model is hard to detect by the instrument adopted in the current simulation at the L2 point. In fact, our further simulations show that a telescope with a minimum aperture of 537 millimeters is required to capture the faint event with a SNR threshold of 3.0.

When the temperature exceeds 3800 K, the droplet model described in Section 3.1 is no longer valid because vapor is believed to be generated upon impact (Cintala, 1992). This case can be covered easily by our simulator by slight modifications. Specifically speaking, the total volume of the vapor produced upon impact can be calculated by Eq. (8), but with different constants provided in Cintala (1992). The radius and the area

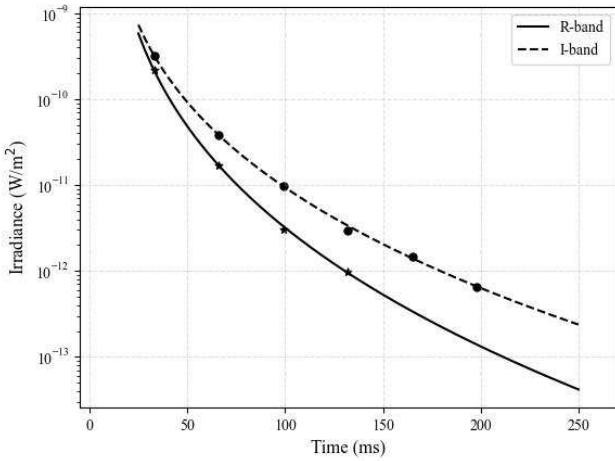


Fig. 5. The modeled evolution of the irradiance, received at the L2 point, of the Flash 2 model. The solid line represents the  $R$ -band light curve, and the dashed line the  $I$ -band. Time = 33 ms marks the first frame, with each subsequent frame spaced 33 ms apart. The overplotted stars and circles correspond to the simulated images shown in Figures 9 and 10, respectively.

of the sphere can then be easily determined by assuming the vapor has a regular spherical shape.

As an example, Figure 11 illustrates the simulated flash images in both  $R$ - and  $I$ -bands for a flash with  $T_0 = 4540 \text{ K}^4$ , for which the mass and velocity of the flash are 13.43 g and 58.35 km/s, respectively. In the current simulation,  $m_\rho$  and  $c_p$  are adopted to be  $0.2 \text{ g/cm}^3$  and  $0.67 \text{ J}\cdot\text{g}^{-1}\cdot\text{K}^{-1}$ , respectively, for gaseous silicon dioxide. The corresponding values of SNR are measured to be 3.40 and 3.81 for the  $R$ - and  $I$ -bands, respectively, which are much lower than the case of the Flash model 2 (Table 5). The low SNR mainly results from a significant decrease of surface area in the vapor model.

Table 5. Values of SNR determined from the simulated images for flash at different moon phases and bands.

Flash	0.1 moon phase		0.5 moon phase	
	$R$ -band	$I$ -band	$R$ -band	$I$ -band
1	0.48	0.66	1.02	1.32
2	228	360	383	525
3	525	567	888	891

## 5. Validation

We validate our simulator in this section by focusing on the three aspects: the background statistics, the simulated PSF and a comparison with the flashes captured on the ground.

### 5.1. Background statistics

Figure 12 (a) and (b) show that distributions of the simulated background at the 0.1 and 0.5 moon phases, respectively, along with the best-fit Poisson distributions. By using the least squares method, the best-fit mean values in ADU are 28521.95, 25529.96, 2522.21, and 2261.09, which are highly consistent with the input values of 28521.86, 25529.95, 2522.20, and 2261.09. The corresponding residual mean squares are calculated to be  $2.6 \times 10^{-7}$ ,  $2.3 \times 10^{-7}$ ,  $2.4 \times 10^{-7}$ , and  $2.1 \times 10^{-7}$ .

### 5.2. PSF profile of the flash

The simulated PSF profiles of the flash 2 model are illustrated in Figure 13. After fitting each simulated PSF by a two-dimensional Gaussian function, Table 6 presents a comparison between the fitting parameters and the inputs, which again indicates a high consistency between the simulated and input PSF.

Table 6. Comparison of the fitted and input PSF in  $R$ - and  $I$ -bands.

Parameters <sup>a</sup>	$G_0$	$x_0$	$y_0$	$\sigma_x$	$\sigma_y$
Input(R)	45202	9.0	9.0	0.80	0.80
Fitted(R)	45515	9.002	8.996	0.7996	0.7938
Input(I)	65535	9.0	9.0	0.80	0.80
Fitted(I)	69031	8.998	9.003	0.8744	0.8750

<sup>a</sup> "Input (R)" or "Input (I)" refers to the input parameters for the  $R$ -band or  $I$ -band, respectively. These parameters are  $G_0$ ,  $x_0$ ,  $y_0$ ,  $\sigma_x$ , and  $\sigma_y$ . Specifically,  $G_0$  is the maximum value at the center of the flash,  $x_0$  and  $y_0$  represent the coordinates of the flash center, and  $\sigma_x$  and  $\sigma_y$  are the dispersion in the  $x$  and  $y$  directions, respectively. "Fitted (R)" or "Fitted (I)" represents the parameters obtained from fitting.

### 5.3. Comparison with ground observations

In order to validate our simulator further, we run the simulator with a series of input models, and compare the results obtained from the simulations with the values measured from the observations. Three flashes (Flash A, D and E) modeled in detail by Yanagisawa & Kisaichi (2002) are adopted in our comparison study. With the modeled parameters listed in Table 7, the total energy per unit area received on the Earth is at first calculated to be  $1.45 \times 10^{-12}$ ,  $8.51 \times 10^{-12}$  and  $1.9 \times 10^{-11} \text{ J m}^{-2}$  for the Flash A, D and E, respectively, which agrees well with the observed values (See Table 7).

We subsequently simulate the images of the flashes A, D, and E using parameters similar to those of the observation system I used in Yanagisawa & Kisaichi (2002), and calculate the corresponding apparent magnitudes by using Vega as the standard star. These calculated magnitudes are compared with the measured brightness provided by Yanagisawa & Kisaichi

<sup>4</sup>The flash No. 43 in Avdellidou & Vaubaillon (2019).

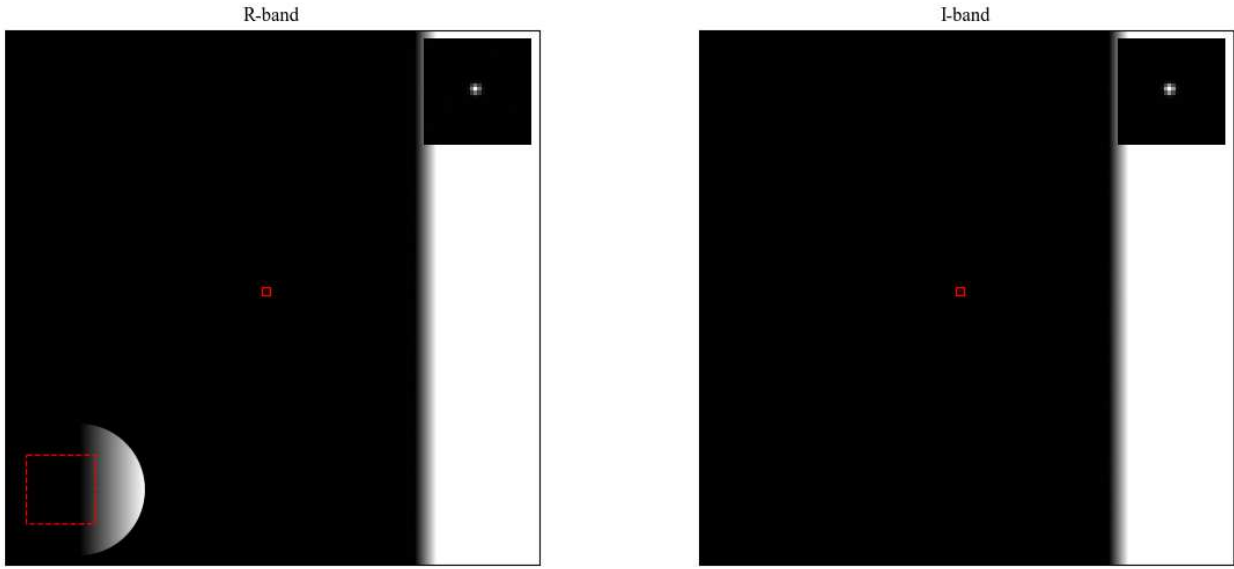


Fig. 6. Simulating a full-size image of  $2048 \times 2048$  pixels at 0.5 moon phase using the flash 2 model. A  $30 \times 30$  pixel window is used to highlight the flash, with the left side displaying the R-band simulated image and the right side showing the I-band simulated image, and both images are the first frame. The corresponding field of view for the entire image is indicated by the red dashed lines in the lower left corner.



Fig. 7. An evolution of the R-band images simulated for the flash 2 model occurring at 0.1 moon phase. The time increases from left to right. Only the  $30 \times 30$  pixels area centered on the flash are displayed in the figure.

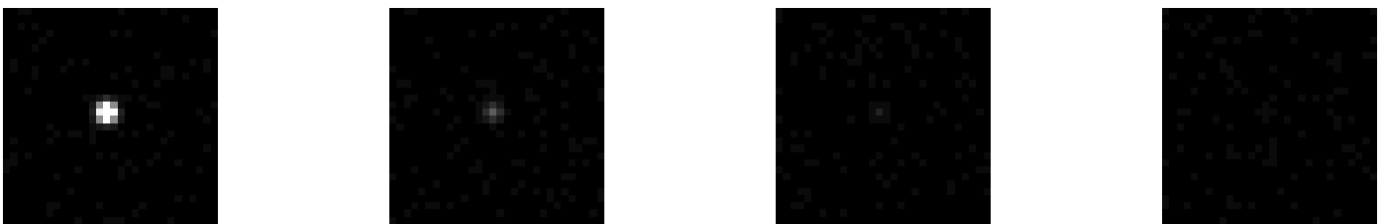


Fig. 8. The same as Figure 7, but for the I-band.



Fig. 9. The same as Figure 7, but for a flash occurring at 0.5 moon phase.

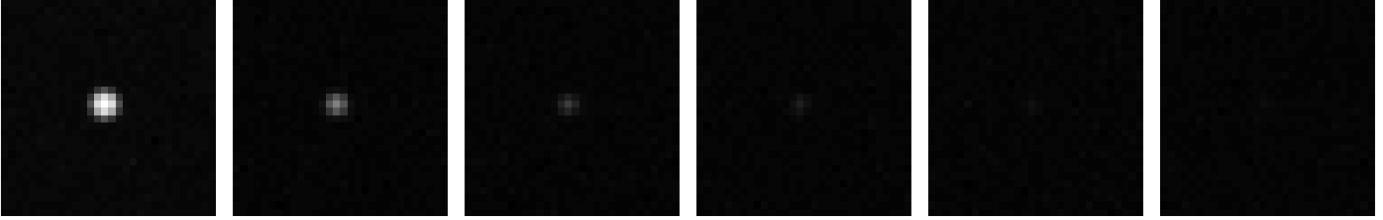


Fig. 10. The same as Figure 9, but for the  $I$ -band.



Fig. 11. Simulated images taken in  $R$ - (panel a) and  $I$ -bands (panel b) of a flash with  $T_0 = 4540\text{K}$ . All the images are simulated at 0.1 moon phase. Due to the SNR being just over 3.0, the flash is difficult to discern by the naked eye, but it can be easily identified using software.

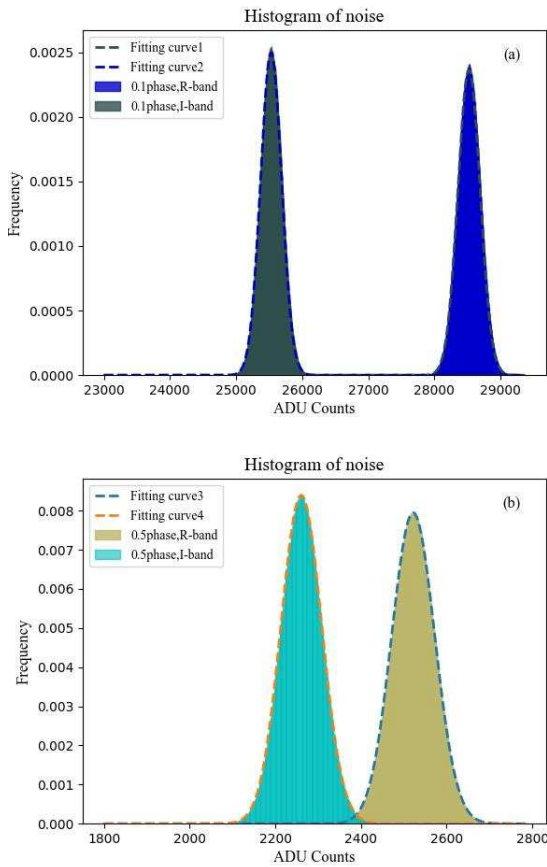


Fig. 12. *Panel (a)*: Distribution of the  $R$ - and  $I$ -bands background levels simulated at the 0.1 moon phase. The best-fit Poisson distributions are over-plotted by the dashed lines; *Panel (b)*: the same as the Panel (a), but for the images simulated at moon phase of 0.5.

(2002) in Table 8. The comparison shows a rough match between the simulated and observed values, which is acceptable because the extinction due to earth atmosphere is not included in our simulator.

## 6. Conclusion and Prospect

In this study, we present an end-to-end image simulator dedicated to capturing impact flashes on lunar far side from space, which is useful for future mission design and optimization. The simulator is designed using a modular approach, developed in Python environment and validated by comparing the simulated results with ground-based observations. The simulator encompasses modules for flash model, background radiation, telescope and detector model.

The modular design enables us to easily improve and update the simulator in the future by adding or replacing more complex physical models in the following aspects:

- Photon counts prediction with spectral energy distributions of both flash and background emission, more detailed and specific flash model and specific transmission of the system.
- More realistic model for the reflection of sunlight by the lunar surface. Rather than the simple Lambert model and the average albedo, the real reflection of lunar surface is complex and depends on lunar topography, morphology, and wavelength.
- Sky background emission. An interface has been designed to incorporate the sky background in the future, which can

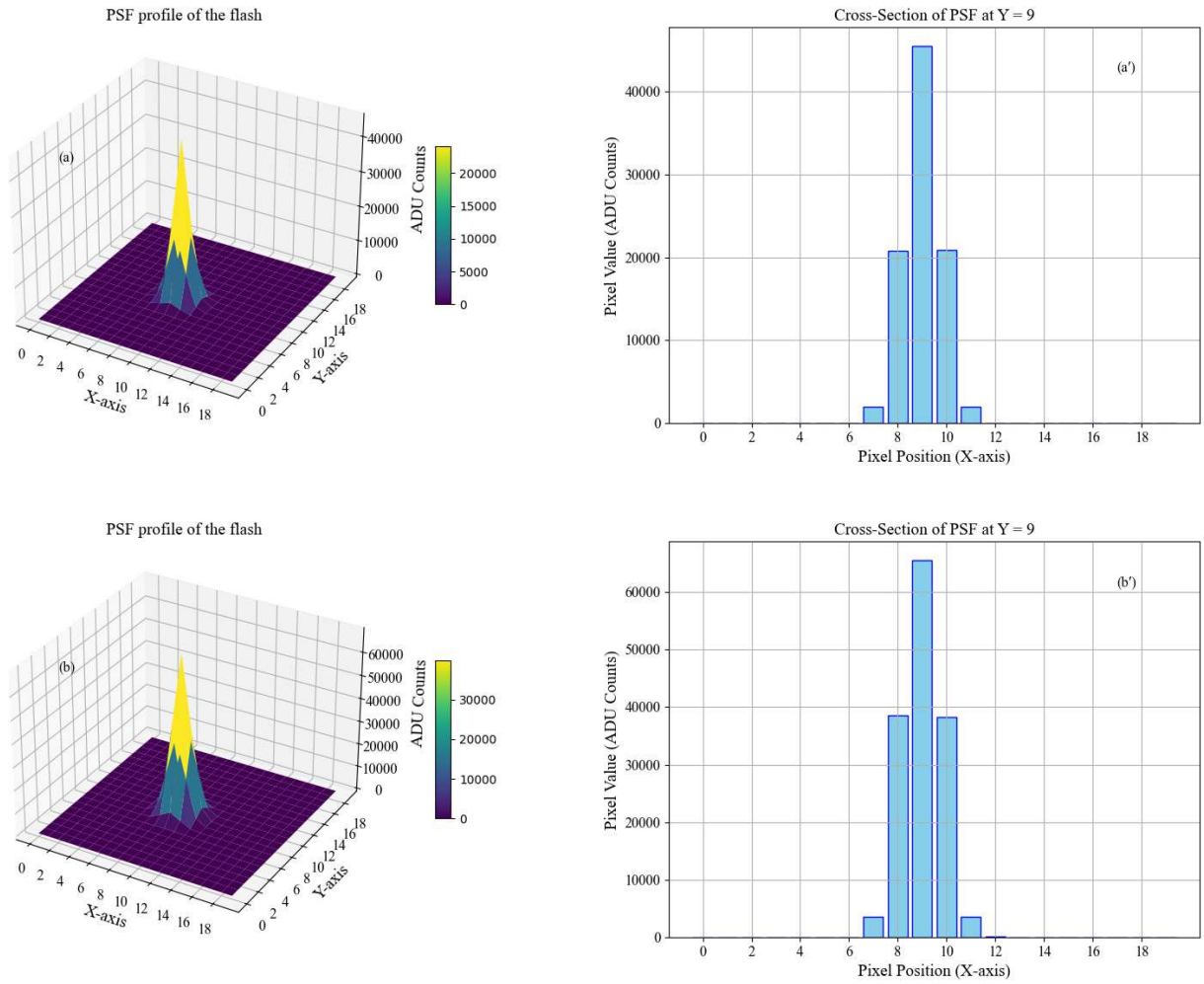


Fig. 13. The simulated PSF in *R*- (panel a) and *I*-bands (panel b) of the first frame images of the flash 2 model. Additionally, we plotted histograms to display the ADU counts of individual pixels. Panel a' and panel b' present the histograms for the R-band and I-band, respectively, both of which are cross-sections taken at  $y = 9$  (where the coordinates of the flash center are (9, 9)).

Table 7. Summary of flash parameters, observed and simulated energy per unit area.

Flash	$T_0$ (K)	$R_d$ ( $\mu\text{m}$ )	$V$ ( $\text{m}^3$ )	$\Phi_{\text{obs}}$ ( $\text{J}/\text{m}^2$ )	$\Phi_{\text{sim}}$ ( $\text{J}/\text{m}^2$ )
A	2100	100	0.05	$2.0 \times 10^{-12}$	$1.45 \times 10^{-12}$
D	2100	150	0.3	$> 7.3 \times 10^{-12}$	$8.51 \times 10^{-12}$
E	2250	180	0.4	$> 1.1 \times 10^{-11}$	$1.90 \times 10^{-11}$

$\Phi_{\text{obs}}$  represents the observed energy per unit area, while  $\Phi_{\text{sim}}$  represents the simulated.

Table 8. Comparison of flash brightness measured from the simulated and observed images.

Flash <sub><i>a</i></sub>	$A_1$	$D_1$	$D_2$	$E_1$	$E_2$	$E_3$	$E_4$
Simulated magnitude	6.32	4.82	5.33	4.05	4.54	4.99	5.41
Observed magnitude	6			$\leq 5$			

<sup>a</sup> The subscript  $i$  denotes the observed  $i$ th image.

create a more complete image that includes the area around the Moon and can also be used for simulating ground-based telescopes, although its level is believed to be much lower than that of lunar surface reflection.

- Imperfect optical system including vignetting, PSF distortion and PST curve either modeled or measured.
- Detector pixel imperfections (Photo Response Non-Uniformity and Dark Signal Non-Uniformity) and dependence of dark current and gain on temperature.
- CCD smear simulation. This simulation models the smear effect introduced by the line-by-line readout process of CCD sensors. During this process, the illuminated part of the Moon may leave residual traces on other lines, particularly under high brightness, degrading image quality. This effect, due to sequential line readout, may not occur with CMOS sensors, which employ a simultaneous frame readout method.

## Acknowledgments

This study is supported by the Natural Science Foundation under grant No. 11973063 and by the Strategic Pioneer Program on Space Science, Chinese Academy of Sciences, grants XDA15072119. JW is supported by Natural Science Foundation of Guangxi (2020GXNSFDA238018). We also sincerely thank the reviewers for their valuable insights and suggestions, which have greatly contributed to improving the quality of this paper.

## Appendix A. Temperatures of the Flashes Observed by NELIOTA

The NELIOTA project, funded by the European Space Agency, has monitored lunar impact flashes in standard Johnson-Cousins  $R$ - and  $I$ -band filters using the 1.2 m Kryoneri telescope located at the National Observatory of Athens, Greece, since 2015 (Bonanos et al., 2018; Xilouris et al., 2018; Liakos et al., 2019). The primary performance of the project are outlined in Table A.9. Its large FoV of  $17.0' \times 14.4'$  enables NELIOTA to monitor up to one-third of the lunar nearside surface. Up to July 2023, a total of 187 events has been detected in both bands within approximately 278 hours observation, which leads to an overall rate of verified flash events of approximately one flash per 1.5 hours.

By assuming a blackbody emission, the temperature of each of the verified flashes reported by NELIOTA can be estimated by us from the flux ratio (Liakos et al., 2020) of the two bands:

$$\frac{f_R}{f_I} = \left( \frac{\lambda_I}{\lambda_R} \right)^5 \cdot \frac{e^{\frac{hc}{\lambda_I k_B T}} - 1}{e^{\frac{hc}{\lambda_R k_B T}} - 1} \quad (\text{A.1})$$

where  $\lambda_R$  and  $\lambda_I$  are the effective wavelengths of the two used filters. With the zero-points of the two bands (Bessell et al., 1998), the flux can be obtained from the corresponding magnitudes,  $m_R$  and  $m_I$ :

$$f_R = 2.18 \times 10^{-8} \times 10^{-0.4m_R} \text{ in } \text{W m}^{-2} \mu\text{m}^{-1} \quad (\text{A.2})$$

$$f_I = 1.13 \times 10^{-8} \times 10^{-0.4m_I} \text{ in } \text{W m}^{-2} \mu\text{m}^{-1} \quad (\text{A.3})$$

We calculate the uncertainty of the estimated temperature by a Monte Carlo simulation with  $10^5$  iterations. In each iteration, a new set of  $m_R$  and  $m_I$  is derived by a random sampling, which is based on the Gaussian distributions defined by the photometric errors in both bands provided by NELIOTA.

The estimated peak temperatures, along with the corresponding uncertainties at  $1\sigma$  significance level, are listed in Table A.10, where we also include flash temperatures calculated by Liakos et al. (2020, 2024). Note that in calculating the flash temperatures, we used the constants from the SciPy library, specifically  $h = 6.62607015 \times 10^{-34} \text{ J}\cdot\text{s}$ ,  $c = 299792458 \text{ m}\cdot\text{s}^{-1}$ , and  $k_B = 1.380649 \times 10^{-23} \text{ J}\cdot\text{K}^{-1}$ . By contrast, Liakos et al.

(2020, 2024) used approximate values:  $h = 6.63 \times 10^{-34} \text{ J} \cdot \text{s}$ ,  $c = 2.998 \times 10^8 \text{ m} \cdot \text{s}^{-1}$ , and  $k_B = 1.38 \times 10^{-23} \text{ J} \cdot \text{K}^{-1}$ . This difference, however, is negligible compared to the original temperature uncertainties.

For most temperatures (182 out of 187), only minor discrepancies are observed. However, we identified five flashes with notable temperature differences: IDs 17, 83, 108, 147, and 181. For ID 17, we found that the flash magnitudes reported by Liakos et al. (2020) in Table A.1 ( $m_R = 10.92$  and  $m_I = 9.20$ ) differ from those on the NELIOTA website ( $m_R = 10.46$  and  $m_I = 9.03$ ), and we used the NELIOTA values. ID 83 corresponds to flash ID 118 in Tables A.1 and A.2 of Liakos et al. (2024). Table A.1 shows differences in magnitudes and magnitude errors for flash IDs 118 and 120, while Table A.2 provides identical calculated values for flash temperature and temperature error for both flashes, which likely indicates an error.

For the remaining flashes with significant temperature differences (IDs 108, 147, and 181), we have not yet identified the cause, but we have conducted thorough checks to ensure the accuracy of our calculations.

Table A.9. The main technical specifications of the NELIOTA telescope.

Optical system parameters		Camera parameters	
Primary mirror	1200 mm	Sensor type	Front-illuminated Scientific CMOS
System focal ratio	$f/2.8$	Sensor size	6.48 m
FoV	$17.0^\circ \times 14.4^\circ$	Shutter	Global
		Valid Pixels	$1280 \times 1080$
		Frame frequency	30 Hz
		Exposure time	23 ms

Table A.10. As of June 22, 2023, NELIOTA has recorded a total of 187 flash events. This table presents the peak magnitudes and occurrence times for each flash as recorded, along with the flash temperatures and their corresponding temperature errors, which were calculated separately by us and Liakos et al. (2020, 2024).

Flash(ID)	Date(UT)	Time(UT)	$R \pm \sigma_R$ (mag)	$I \pm \sigma_I$ (mag)	$T \pm \sigma_T$ (K)	$T \pm \sigma_T$ (K) (Liakos et al., 2020, 2024)
1	2017/2/1	17:13:58	10.15±0.12	9.05±0.05	3047±263	3046±307
2	2017/3/1	17:08:47	6.67±0.07	6.07±0.06	4509±427	4503±646
3	2017/3/1	17:13:17	9.15±0.11	8.23±0.07	3445±341	3438±431
4	2017/3/4	20:51:32	9.5±0.14	8.79±0.06	4073±598	4076±748
5	2017/4/1	19:45:52	10.18±0.13	8.61±0.03	2344±156	2343±200
6	2017/5/1	20:30:58	10.19±0.18	8.84±0.05	2627±283	2615±315
7	2017/6/27	18:58:27	11.07±0.32	9.27±0.06	2107±330	2101±343
8	2017/6/28	18:45:26	10.56±0.38	9.48±0.13	3086±1059	3088±945
9	2017/7/19	2:00:36	11.23±0.4	9.33±0.06	2018±397	2008±367
10	2017/7/28	18:21:45	11.24±0.34	9.29±0.06	1977±309	1978±300
11	2017/7/28	18:42:58	10.72±0.24	9.63±0.1	3067±591	3056±647
12	2017/7/28	18:51:42	10.84±0.24	9.81±0.09	3190±644	3168±692
13	2017/7/28	19:17:18	8.27±0.04	6.32±0.01	1977±34	1972±105
14	2017/8/16	1:05:47	10.15±0.18	9.54±0.1	4466±1048	4455±1146
15	2017/8/16	2:15:59	10.69±0.28	9.11±0.06	2333±357	2326±356
16	2017/8/16	2:41:15	10.81±0.3	9.08±0.06	2174±330	2167±319
17	2017/8/18	2:02:21	10.46±0.02	9.03±0.02	2517±37	2185±255
18	2017/8/18	2:03:08	10.19±0.12	8.83±0.04	2613±184	2615±256
19	2017/9/14	3:17:50	9.17±0.07	8.07±0.03	3047±150	3058±207
20	2017/9/16	2:26:25	8.52±0.03	7.04±0.01	2452±40	2440±136
21	2017/10/13	1:54:22	9.28±0.11	8.37±0.04	3471±309	3458±357
22	2017/10/13	2:33:44	10.31±0.24	9.89±0.12	5494±1534	5453±1740
23	2017/10/16	2:46:46	10.72±0.16	9.46±0.05	2764±280	2751±384
24	2017/10/26	17:59:43	10.03±0.25	9.42±0.12	4466±1341	4431±1088
25	2017/11/14	3:34:15	10.31±0.17	9.31±0.06	3256±435	3264±488
26	2017/11/23	16:17:33	10.45±0.23	10.06±0.12	5706±1541	5722±1528
27	2017/12/12	2:48:08	10.5±0.24	8.98±0.08	2403±327	2402±334
28	2017/12/12	4:30:01	10.58±0.28	9.84±0.11	3969±1225	3948±1267
29	2017/12/13	4:26:58	10.56±0.23	9.95±0.11	4466±1261	4432±1475
30	2017/12/14	4:35:10	7.94±0.05	6.76±0.02	2899±95	2889±200
31	2018/1/12	3:54:03	10.01±0.14	9.31±0.07	4109±630	4101±782
32	2018/3/23	17:24:19	9.93±0.26	8.62±0.06	2686±450	2675±431
33	2018/4/10	3:36:58	8.84±0.13	8.08±0.05	3903±486	3905±626
34	2018/6/9	2:29:18	9.92±0.23	9±0.09	3445±740	3428±727
35	2018/6/19	19:12:10	9.87±0.21	9.03±0.09	3659±766	3646±736
36	2018/6/19	20:00:48	9.92±0.28	9.31±0.14	4466±1444	4436±1094
37	2018/6/19	20:04:10	10.26±0.61	8.63±0.11	2277±980	2267±695
38	2018/7/9	1:44:19	11.16±0.28	10.06±0.12	3047±722	3032±748
39	2018/8/6	1:57:44	9.68±0.16	8.14±0.04	2379±200	2369±215
40	2018/8/6	2:38:14	9.16±0.09	7.73±0.02	2517±123	2515±156
41	2018/8/7	1:33:55	10.79±0.26	9.31±0.07	2452±370	2444±405
42	2018/8/7	1:35:45	8.78±0.05	7.74±0.02	3169±115	3153±262
43	2018/8/7	2:33:18	10.07±0.17	9.46±0.07	4466±920	4460±988
44	2018/8/7	3:10:33	10.39±0.31	9.8±0.14	4554±1527	4558±1087
45	2018/8/8	2:19:55	11.14±0.28	9.9±0.07	2797±548	2793±583
46	2018/8/8	2:28:23	11.06±0.21	10.4±0.13	4260±1147	4253±1364
47	2018/8/8	2:29:45	8.36±0.04	7.3±0.02	3127±93	3124±247



Flash(ID)	Date(UT)	Time(UT)	R $\pm$ $\sigma_R$ (mag)	I $\pm$ $\sigma_I$ (mag)	T $\pm$ $\sigma_T$ (K)	T $\pm$ $\sigma_T$ (K) (Liakos et al., 2020, 2024)
48	2018/8/8	2:52:26	11.05 $\pm$ 0.31	9.74 $\pm$ 0.1	2686 $\pm$ 588	2678 $\pm$ 563
49	2018/8/15	18:08:17	11.8 $\pm$ 0.36	9.56 $\pm$ 0.09	1765 $\pm$ 262	1758 $\pm$ 257
50	2018/9/4	1:33:53	9.87 $\pm$ 0.3	9.18 $\pm$ 0.1	4145 $\pm$ 1346	4163 $\pm$ 1490
51	2018/9/5	1:51:37	7.84 $\pm$ 0.07	6.6 $\pm$ 0.02	2797 $\pm$ 120	2793 $\pm$ 194
52	2018/9/5	2:47:54	10.61 $\pm$ 0.37	9.09 $\pm$ 0.09	2403 $\pm$ 552	2401 $\pm$ 501
53	2018/9/6	2:00:33	10.95 $\pm$ 0.3	10.33 $\pm$ 0.14	4423 $\pm$ 1469	4428 $\pm$ 1348
54	2018/9/6	3:10:04	11.18 $\pm$ 0.25	9.86 $\pm$ 0.09	2671 $\pm$ 443	2660 $\pm$ 459
55	2018/10/15	18:17:49	9.61 $\pm$ 0.17	8.84 $\pm$ 0.08	3870 $\pm$ 683	3836 $\pm$ 787
56	2019/2/9	17:29:38	10.32 $\pm$ 0.28	9.91 $\pm$ 0.14	5563 $\pm$ 1628	5601 $\pm$ 1560
57	2019/2/9	18:17:00	10.39 $\pm$ 0.25	9.82 $\pm$ 0.12	4646 $\pm$ 1396	4647 $\pm$ 1169
58	2019/4/10	19:53:21	9.45 $\pm$ 0.26	8.55 $\pm$ 0.1	3496 $\pm$ 886	3506 $\pm$ 868
59	2019/6/8	19:14:59	10.08 $\pm$ 0.37	8.64 $\pm$ 0.08	2503 $\pm$ 608	2499 $\pm$ 522
60	2019/6/8	19:26:58	9.24 $\pm$ 0.16	8.04 $\pm$ 0.05	2864 $\pm$ 302	2864 $\pm$ 298
61	2019/6/28	1:56:48	8.88 $\pm$ 0.06	7.59 $\pm$ 0.02	2717 $\pm$ 98	2709 $\pm$ 215
62	2019/6/28	2:18:23	10.12 $\pm$ 0.18	9.29 $\pm$ 0.08	3688 $\pm$ 647	3678 $\pm$ 715
63	2019/7/6	19:12:55	10.06 $\pm$ 0.21	9.08 $\pm$ 0.08	3301 $\pm$ 588	3307 $\pm$ 644
64	2019/7/7	18:32:56	10.94 $\pm$ 0.34	9.63 $\pm$ 0.09	2686 $\pm$ 654	2678 $\pm$ 590
65	2019/7/7	18:40:21	6.65 $\pm$ 0.06	5.49 $\pm$ 0.03	2934 $\pm$ 122	2922 $\pm$ 205
66	2019/7/7	18:48:48	11.94 $\pm$ 0.54	9.86 $\pm$ 0.1	1876 $\pm$ 519	1873 $\pm$ 405
67	2019/7/8	19:11:44	9.77 $\pm$ 0.2	8.19 $\pm$ 0.08	2333 $\pm$ 257	2325 $\pm$ 266
68	2019/7/26	0:18:28	10.75 $\pm$ 0.3	9.65 $\pm$ 0.13	3047 $\pm$ 799	3036 $\pm$ 790
69	2019/7/26	0:41:35	9.64 $\pm$ 0.14	8.21 $\pm$ 0.03	2517 $\pm$ 193	2510 $\pm$ 239
70	2019/7/27	1:13:12	10.68 $\pm$ 0.32	9.46 $\pm$ 0.08	2830 $\pm$ 680	2817 $\pm$ 646
71	2019/7/27	1:17:50	8.95 $\pm$ 0.09	8.02 $\pm$ 0.03	3420 $\pm$ 240	3404 $\pm$ 368
72	2019/7/27	2:12:25	9.67 $\pm$ 0.16	8.67 $\pm$ 0.05	3256 $\pm$ 399	3273 $\pm$ 441
73	2019/7/27	2:37:23	10.16 $\pm$ 0.2	9.48 $\pm$ 0.06	4183 $\pm$ 932	4186 $\pm$ 953
74	2019/7/27	2:59:56	9.48 $\pm$ 0.16	8.25 $\pm$ 0.06	2813 $\pm$ 295	2896 $\pm$ 697
75	2019/7/27	3:01:26	8.9 $\pm$ 0.12	7.47 $\pm$ 0.04	2517 $\pm$ 170	2503 $\pm$ 197
76	2019/7/28	1:33:40	10.08 $\pm$ 0.14	8.93 $\pm$ 0.06	2952 $\pm$ 290	2941 $\pm$ 386
77	2019/7/28	1:59:21	10.8 $\pm$ 0.27	9.62 $\pm$ 0.1	2899 $\pm$ 598	2879 $\pm$ 611
78	2019/7/28	2:00:54	11.37 $\pm$ 0.32	10.51 $\pm$ 0.14	3603 $\pm$ 1198	3592 $\pm$ 1243
79	2019/7/28	2:24:26	11.04 $\pm$ 0.26	9.93 $\pm$ 0.09	3027 $\pm$ 626	3004 $\pm$ 633
80	2019/8/6	18:19:16	10.37 $\pm$ 0.27	8.71 $\pm$ 0.12	2245 $\pm$ 340	2237 $\pm$ 317
81	2019/8/6	18:56:37	8.43 $\pm$ 0.08	7.38 $\pm$ 0.04	3148 $\pm$ 189	3151 $\pm$ 305
82	2019/8/6	18:59:16	9.34 $\pm$ 0.09	9 $\pm$ 0.07	6104 $\pm$ 1025	6149 $\pm$ 1410
83	2019/8/26	2:50:56	10.65 $\pm$ 0.24	9.11 $\pm$ 0.05	2379 $\pm$ 309	2933 $\pm$ 600
84	2019/8/28	3:03:31	10.98 $\pm$ 0.26	9.82 $\pm$ 0.14	2934 $\pm$ 638	2933 $\pm$ 600
85	2019/9/5	18:11:59	10.13 $\pm$ 0.19	9.52 $\pm$ 0.1	4466 $\pm$ 1090	4443 $\pm$ 1207
86	2019/9/5	18:51:33	10.25 $\pm$ 0.25	9.53 $\pm$ 0.14	4038 $\pm$ 1204	4016 $\pm$ 1214
87	2019/9/23	3:36:22	10.2 $\pm$ 0.28	9.4 $\pm$ 0.1	3777 $\pm$ 1119	3777 $\pm$ 1042
88	2019/9/25	3:40:11	8.43 $\pm$ 0.05	7.42 $\pm$ 0.02	3234 $\pm$ 120	3212 $\pm$ 207
89	2019/10/22	4:11:36	10 $\pm$ 0.17	9.28 $\pm$ 0.1	4038 $\pm$ 802	4036 $\pm$ 810
90	2019/10/24	2:30:16	9.49 $\pm$ 0.12	7.88 $\pm$ 0.03	2299 $\pm$ 138	2288 $\pm$ 160
91	2019/11/2	17:19:20	10.22 $\pm$ 0.27	9.26 $\pm$ 0.1	3348 $\pm$ 842	3345 $\pm$ 770
92	2019/11/3	17:49:38	9.61 $\pm$ 0.21	8.77 $\pm$ 0.1	3659 $\pm$ 782	3641 $\pm$ 770
93	2019/12/1	16:14:30	9.17 $\pm$ 0.13	8.46 $\pm$ 0.1	4073 $\pm$ 652	4080 $\pm$ 647

Flash(ID)	Date(UT)	Time(UT)	R $\pm$ $\sigma_R$ (mag)	I $\pm$ $\sigma_I$ (mag)	T $\pm$ $\sigma_T$ (K)	T $\pm$ $\sigma_T$ (K) (Liakos et al., 2020, 2024)
94	2019/12/1	16:23:14	8.42 $\pm$ 0.06	5.57 $\pm$ 0.04	1442 $\pm$ 31	1438 $\pm$ 53
95	2019/12/1	16:30:43	10.75 $\pm$ 0.24	9.12 $\pm$ 0.13	2277 $\pm$ 319	2277 $\pm$ 353
96	2019/12/1	17:14:41	11.16 $\pm$ 0.36	9.35 $\pm$ 0.13	2098 $\pm$ 403	2093 $\pm$ 363
97	2019/12/20	4:34:17	9.5 $\pm$ 0.19	8.51 $\pm$ 0.06	3278 $\pm$ 496	3254 $\pm$ 477
98	2020/1/30	17:18:09	11.03 $\pm$ 0.31	9.51 $\pm$ 0.11	2403 $\pm$ 453	2393 $\pm$ 427
99	2020/1/30	17:35:39	10.62 $\pm$ 0.19	9.75 $\pm$ 0.11	3576 $\pm$ 684	3558 $\pm$ 727
100	2020/3/1	16:54:24	8.32 $\pm$ 0.06	7.15 $\pm$ 0.02	2916 $\pm$ 113	2919 $\pm$ 161
101	2020/3/1	17:10:06	9.92 $\pm$ 0.25	9.42 $\pm$ 0.12	5004 $\pm$ 1477	4991 $\pm$ 2002
102	2020/3/27	17:40:25	10.01 $\pm$ 0.12	8.7 $\pm$ 0.04	2686 $\pm$ 195	2677 $\pm$ 263
103	2020/3/29	18:14:11	10.83 $\pm$ 0.2	9.72 $\pm$ 0.08	3027 $\pm$ 457	3030 $\pm$ 507
104	2020/3/29	19:16:47	10.18 $\pm$ 0.19	9.26 $\pm$ 0.06	3445 $\pm$ 560	3430 $\pm$ 605
105	2020/4/28	19:19:55	8.99 $\pm$ 0.07	8.13 $\pm$ 0.02	3603 $\pm$ 204	3587 $\pm$ 323
106	2020/6/25	18:28:18	7.92 $\pm$ 0.07	6.66 $\pm$ 0.03	2764 $\pm$ 123	2763 $\pm$ 192
107	2020/6/26	19:52:32	9.73 $\pm$ 0.07	8.22 $\pm$ 0.02	2415 $\pm$ 89	2408 $\pm$ 160
108	2020/7/26	19:08:21	10.2 $\pm$ 0.09	9.13 $\pm$ 0.1	3107 $\pm$ 282	2788 $\pm$ 365
109	2020/7/26	19:10:25	9.15 $\pm$ 0.04	7.82 $\pm$ 0.02	2657 $\pm$ 66	2649 $\pm$ 171
110	2020/8/13	0:57:11	10.16 $\pm$ 0.24	9.03 $\pm$ 0.07	2989 $\pm$ 532	2991 $\pm$ 540
111	2020/8/14	0:54:21	9.29 $\pm$ 0.12	8.53 $\pm$ 0.05	3903 $\pm$ 449	3910 $\pm$ 623
112	2020/8/14	1:15:36	9.95 $\pm$ 0.18	9.45 $\pm$ 0.1	5004 $\pm$ 1242	4961 $\pm$ 1518
113	2020/12/9	3:09:58	9.83 $\pm$ 0.17	9.32 $\pm$ 0.09	4949 $\pm$ 1159	4967 $\pm$ 1227
114	2021/3/17	17:46:53	9.48 $\pm$ 0.1	7.97 $\pm$ 0.03	2415 $\pm$ 129	2410 $\pm$ 168
115	2021/3/17	18:07:19	10.47 $\pm$ 0.21	9.21 $\pm$ 0.06	2764 $\pm$ 376	2754 $\pm$ 391
116	2021/4/18	19:13:59	9.43 $\pm$ 0.13	7.89 $\pm$ 0.04	2379 $\pm$ 164	2370 $\pm$ 184
117	2021/4/18	20:19:24	9.74 $\pm$ 0.19	8.64 $\pm$ 0.08	3047 $\pm$ 437	3038 $\pm$ 460
118	2021/5/15	18:38:41	10.12 $\pm$ 0.2	9.38 $\pm$ 0.08	3969 $\pm$ 865	3971 $\pm$ 926
119	2021/5/18	20:08:22	9.9 $\pm$ 0.19	8.66 $\pm$ 0.06	2797 $\pm$ 348	2788 $\pm$ 365
120	2021/6/15	19:06:13	9.96 $\pm$ 0.13	9.19 $\pm$ 0.06	3870 $\pm$ 492	3863 $\pm$ 596
121	2021/6/15	19:23:19	10.86 $\pm$ 0.28	10.19 $\pm$ 0.16	4221 $\pm$ 1391	4457 $\pm$ 1492
122	2021/6/15	19:38:52	8.15 $\pm$ 0.05	6.73 $\pm$ 0.02	2530 $\pm$ 72	2520 $\pm$ 158
123	2021/7/6	2:11:11	10.82 $\pm$ 0.08	10.33 $\pm$ 0.15	5060 $\pm$ 1082	5070 $\pm$ 1586
124	2021/7/15	19:22:29	10.2 $\pm$ 0.26	8.76 $\pm$ 0.07	2503 $\pm$ 388	2497 $\pm$ 385
125	2021/7/16	18:49:32	9.96 $\pm$ 0.33	9.15 $\pm$ 0.11	3747 $\pm$ 1263	3746 $\pm$ 1274
126	2021/8/2	1:26:06	10.41 $\pm$ 0.28	9.85 $\pm$ 0.13	4694 $\pm$ 1488	4646 $\pm$ 1967
127	2021/8/2	1:34:28	8.75 $\pm$ 0.16	8.28 $\pm$ 0.08	5176 $\pm$ 1169	5171 $\pm$ 1433
128	2021/8/2	2:44:36	10.12 $\pm$ 0.25	9.72 $\pm$ 0.15	5634 $\pm$ 1595	5634 $\pm$ 2105
129	2021/8/2	2:51:03	8.85 $\pm$ 0.15	7.74 $\pm$ 0.04	3027 $\pm$ 313	3022 $\pm$ 349
130	2021/10/3	3:14:17	10.17 $\pm$ 0.17	9.37 $\pm$ 0.07	3777 $\pm$ 627	3791 $\pm$ 726
131	2021/10/11	16:57:00	8.66 $\pm$ 0.08	7.73 $\pm$ 0.03	3420 $\pm$ 215	3404 $\pm$ 385
132	2021/10/12	16:31:16	9.33 $\pm$ 0.21	8.25 $\pm$ 0.08	3086 $\pm$ 502	3066 $\pm$ 516
133	2021/10/12	17:42:18	9.75 $\pm$ 0.17	8.75 $\pm$ 0.07	3256 $\pm$ 445	3248 $\pm$ 528
134	2021/12/8	16:15:11	8.58 $\pm$ 0.09	7.59 $\pm$ 0.04	3278 $\pm$ 227	3261 $\pm$ 322
135	2021/12/8	16:34:22	10.17 $\pm$ 0.3	8.2 $\pm$ 0.05	1960 $\pm$ 260	1953 $\pm$ 252
136	2022/4/5	17:30:56	8.87 $\pm$ 0.15	7.53 $\pm$ 0.05	2642 $\pm$ 240	2635 $\pm$ 265
137	2022/4/5	17:54:38	9.31 $\pm$ 0.13	7.95 $\pm$ 0.05	2613 $\pm$ 204	2600 $\pm$ 232
138	2022/6/3	18:21:31	7.96 $\pm$ 0.09	6.64 $\pm$ 0.02	2671 $\pm$ 139	2666 $\pm$ 192
139	2022/6/4	18:20:51	9.4 $\pm$ 0.27	8.32 $\pm$ 0.08	3086 $\pm$ 671	3081 $\pm$ 624

Flash(ID)	Date(UT)	Time(UT)	$R \pm \sigma_R(\text{mag})$	$I \pm \sigma_I(\text{mag})$	$T \pm \sigma_T(\text{K})$	$T \pm \sigma_T(\text{K})$ (Liakos et al., 2020, 2024)
140	2022/6/4	18:22:47	10.15±0.38	9.19±0.14	3347±1229	3326±1077
141	2022/6/4	19:44:17	10.06±0.29	9.45±0.14	4466±1473	4477±1909
142	2022/6/23	1:46:08	8.73±0.12	7.22±0.03	2415±154	2409±207
143	2022/7/22	2:13:27	9.97±0.23	8.73±0.06	2797±427	2788±425
144	2022/7/22	2:48:11	10.27±0.35	9.29±0.13	3301±1114	3297±993
145	2022/7/22	2:49:51	9.36±0.28	7.51±0.09	2062±281	2056±257
146	2022/8/1	18:27:23	9.93±0.25	8.66±0.12	2748±498	2744±516
147	2022/8/1	18:28:19	9.42±0.18	7.62±0.1	2107±197	2435±410
148	2022/8/3	18:23:43	9.76±0.08	8.37±0.05	2571±132	2575±204
149	2022/8/4	18:47:07	9.26±0.16	7.63±0.11	2277±217	2271±242
150	2022/9/1	18:33:36	10.66±0.27	8.04±0.05	1549±141	1543±186
151	2022/10/19	3:03:44	8.47±0.08	8.25±0.04	7372±1028	7426±1907
152	2022/10/20	1:12:58	8.58±0.1	7.38±0.02	2864±178	2858±285
153	2022/10/20	2:56:38	9.08±0.08	8.59±0.04	5060±539	5084±755
154	2022/10/21	2:55:12	10.22±0.22	9.56±0.07	4260±1071	4254±1213
155	2022/10/22	3:07:57	10.92±0.23	10.27±0.13	4299±1231	4285±1532
156	2022/10/22	3:25:18	10.44±0.06	9.55±0.11	3522±343	3512±466
157	2022/10/22	3:39:55	10.7±0.06	9.91±0.03	3807±210	3800±543
158	2022/10/22	3:55:36	9.51±0.12	8.68±0.05	3688±396	3677±488
159	2022/10/22	3:56:50	10.31±0.24	9.51±0.09	3777±954	3778±935
160	2022/10/29	17:03:58	9.25±0.12	7.72±0.03	2391±150	2382±279
161	2022/10/30	16:41:06	10.08±0.28	9.26±0.12	3717±1120	3711±1109
162	2022/10/30	16:47:28	9.68±0.19	8.56±0.05	3008±402	3005±472
163	2022/10/30	16:54:55	9.65±0.16	8.57±0.05	3086±356	3080±453
164	2022/10/30	17:34:16	8.64±0.08	8.03±0.05	4466±427	4475±883
165	2022/10/31	19:17:17	8.6±0.16	7.51±0.05	3067±349	3065±517
166	2022/11/19	2:39:28	8.82±0.13	7.92±0.05	3496±382	3492±462
167	2022/12/18	3:37:48	9.11±0.13	7.74±0.04	2599±197	2577±225
168	2022/12/26	15:46:17	7.76±0.07	6.38±0.05	2585±121	2579±197
169	2022/12/26	16:48:14	10.26±0.17	9.68±0.08	4600±1004	4580±1240
170	2022/12/27	16:18:50	9.64±0.2	9.08±0.11	4694±1239	4669±1310
171	2022/12/27	17:47:37	9.29±0.14	7.98±0.05	2686±232	2675±298
172	2022/12/27	18:11:32	9.73±0.04	8.53±0.1	2864±188	2856±307
173	2023/1/16	4:11:21	10.09±0.25	9.04±0.08	3148±641	3144±623
174	2023/2/22	17:49:41	10.37±0.15	10.15±0.1	7372±1406	7336±2244
175	2023/2/22	17:52:04	9.97±0.12	8.7±0.03	2748±200	2745±381
176	2023/3/26	20:25:29	9.88±0.15	8.79±0.05	3067±328	3054±428
177	2023/4/23	18:04:40	10.6±0.18	9.61±0.09	3278±503	3260±600
178	2023/4/24	17:58:31	10.47±0.31	9.1±0.07	2599±518	2597±485
179	2023/4/24	20:02:42	9.63±0.22	8.28±0.06	2627±353	2630±400
180	2023/5/23	20:06:15	8.94±0.09	8.16±0.04	3839±320	3860±681
181	2023/5/24	20:11:10	8.32±0.05	6.41±0.01	2010±43	2824±237
182	2023/5/24	21:03:20	9.1±0.09	7.53±0.02	2344±106	2335±262
183	2023/5/25	20:34:28	7.51±0.03	6.28±0.01	2813±52	2935±465
184	2023/5/26	18:17:44	9.79±0.37	8.25±0.08	2379±538	2376±469
185	2023/6/21	18:47:44	9.21±0.06	9±0.04	7505±914	7520±2682
186	2023/6/22	19:58:09	11±0.29	10.24±0.13	3903±1247	3911±1643
187	2023/6/22	20:03:20	10.18±0.14	8.53±0.03	2256±155	2372±375

## References

- Avdellidou, C., & Vaubaillon, J. (2019). Temperatures of lunar impact flashes: mass and size distribution of small impactors hitting the moon. *Monthly Notices of the Royal Astronomical Society*, 484(4), 5212–5222.
- Bessell, M., Castelli, F., & Plez, B. (1998). Model atmospheres broad-band colors, bolometric corrections and temperature calibrations for o-m stars. *Astronomy and Astrophysics*, v. 333, p. 231-250 (1998), 333, 231–250.
- Bonanos, A., Avdellidou, C., Liakos, A. et al. (2018). Neliota: First temperature measurement of lunar impact flashes. *Astronomy & Astrophysics*, 612, A76.
- Bonanos, A., Xilouris, M., Boumies, P. et al. (2015). Neliota: Esa's new neo lunar impact monitoring project with the 1.2 m telescope at the national observatory of athens. *Proceedings of the International Astronomical Union*, 10(S318), 327–329.
- Bouley, S., Baratoux, D., Vaubaillon, J. et al. (2012). Power and duration of impact flashes on the moon: Implication for the cause of radiation. *Icarus*, 218(1), 115–124.
- Burns, J. O., Kring, D. A., Hopkins, J. B. et al. (2013). A lunar l2-farside exploration and science mission concept with the orion multi-purpose crew vehicle and a teleoperated lander/rover. *Advances in space research*, 52(2), 306–320.
- Cao, L., & Wang, S. (2020). The lunar impact flash observations and research. *Progress in Astronomy*, 38, 255–271.
- Cervone, A., Topputo, F., Speretta, S. et al. (2022). Lumio: A cubesat for observing and characterizing micro-meteoroid impacts on the lunar far side. *Acta Astronautica*, 195, 309–317.
- Cintala, M. J. (1992). Impact-induced thermal effects in the lunar and mercurian regoliths. *Journal of Geophysical Research: Planets*, 97(E1), 947–973.
- Cooke, W., Suggs, R., Suggs, R. et al. (2007). Rate and distribution of kilogram lunar impactors. In *38th Annual Lunar and Planetary Science Conference* 1338 (p. 1986).
- Cooke, W. J., Suggs, R., & Swift, W. R. (2006). A probable taurid impact on the moon. In *2006 Lunar and Planetary Science Conference*.
- Davis, D. R., Durda, D. D., Marzari, F. et al. (2002). Collisional evolution of small-body populations. *Asteroids III*, 545.
- Drolshagen, E., Ott, T., Koschny, D. et al. (2020). Velocity distribution of larger meteoroids and small asteroids impacting earth. *Planetary and Space Science*, 184, 104869.
- Dunham, D., Cudnik, B., Hendrix, S. et al. (1999). Lunar leonid meteors; dd cir. *International Astronomical Union Circular*, 7320, 1.
- Elphic, R., Delory, G., Colaprete, A. et al. (2011). Nasa's lunar atmosphere and dust environment explorer (ladee). In *Geophysical Research Abstracts*. volume 13.
- Gordon, J. (1921). Meteors on the moon. *Nature*, 107(2686), 234–235.
- Harris, C. R., Millman, K. J., Van Der Walt, S. J. et al. (2020). Array programming with numpy. *Nature*, 585(7825), 357–362.
- Heiken, G., Vaniman, D., & French, B. M. (1991). *Lunar sourcebook: A user's guide to the Moon*. 1259. Cup Archive.
- Horanyi, M., Sternovsky, Z., Lankton, M. et al. (2015). The lunar dust experiment (ldex) onboard the lunar atmosphere and dust environment explorer (ladee) mission. *The Lunar Atmosphere and Dust Environment Explorer Mission (LADEE)*, (pp. 93–113).
- Konnik, M., & Welsh, J. (2014). High-level numerical simulations of noise in ccd and cmos photosensors: review and tutorial. *arXiv preprint arXiv:1412.4031*, .
- Lambert, J. H. (1760). *Photometria sive de mensura et gradibus luminis, colorum et umbrae*. sumptibus viduae E. Klett, typis CP Dettleffsen.
- Liakos, A., Bonanos, A., Xilouris, E. et al. (2019). Neliota lunar impact flash detection and event validation. *arXiv preprint arXiv:1901.11414*, .
- Liakos, A., Bonanos, A., Xilouris, E. et al. (2020). Neliota: Methods, statistics, and results for meteoroids impacting the moon. *Astronomy & Astrophysics*, 633, A112.
- Liakos, A., Bonanos, A. Z., Xilouris, E. M. et al. (2024). Neliota: New results and updated statistics after 6.5 years of lunar impact flashes monitoring. *Astronomy & Astrophysics*, .
- Madiedo, J. M., Trigo-Rodríguez, J. M., Ortiz, J. L. et al. (2010). Robotic systems for meteor observing and moon impact flashes detection in spain. *Advances in Astronomy*, 2010.
- McKay, D. S., Heiken, G., Basu, A. et al. (1991). The lunar regolith. *Lunar sourcebook*, 567, 285–356.
- Merisio, G., & Topputo, F. (2023). Present-day model of lunar meteoroids and their impact flashes for lumio mission. *Icarus*, 389, 115180.
- Moser, D., Suggs, R., Swift, W. et al. (2011). Luminous efficiency of hypervelocity meteoroid impacts on the moon derived from the 2006 geminids, 2007 lyrids, and 2008 taurids. *Meteoroids: The Smallest Solar System Bodies*, .
- Muinenen, K., Parviainen, H., Näränen, J. et al. (2011). Lunar mare single-scattering, porosity, and surface-roughness properties with smart-1 amie. *Astronomy & Astrophysics*, 531, A150.
- Ortiz, J., Aceituno, F., Quesada, J. et al. (2006). Detection of sporadic impact flashes on the moon: Implications for the luminous efficiency of hypervelocity impacts and derived terrestrial impact rates. *Icarus*, 184(2), 319–326.
- Ortiz, J., Quesada, J., Aceituno, J. et al. (2002). Observation and interpretation of leonid impact flashes on the moon in 2001. *The Astrophysical Journal*, 576(1), 567.
- Ortiz, J., Sada, P., Bellot Rubio, L. et al. (2000). Optical detection of meteoroidal impacts on the moon. *Nature*, 405(6789), 921–923.
- Pokorný, P., Janches, D., Sarantos, M. et al. (2019). Meteoroids at the moon: orbital properties, surface vaporization, and impact ejecta production. *Journal of Geophysical Research: Planets*, 124(3), 752–778.
- Raab, H. (2002). Detecting and measuring faint point sources with a ccd. In *Proceedings of Meeting on Asteroids and Comets in Europe (MACE)(Visnjam)* (pp. 1–12). Citeseer.
- Robitaille, T. P., Tollerud, E. J., Greenfield, P. et al. (2013). Astropy: A community python package for astronomy. *Astronomy & Astrophysics*, 558, A33.
- Sholl, M., Grochocki, F., Fleming, J. et al. (2007). Stray light design and analysis of the snap telescope. In *Optical Modeling and Performance Predictions III* (pp. 128–139). SPIE volume 6675.
- Stephens, G. L., O'Brien, D., Webster, P. J. et al. (2015). The albedo of earth. *Reviews of geophysics*, 53(1), 141–163.
- Stuart, L. H. (1956). A photo-visual observation of an impact of a large meteorite on the moon. *Strolling Astronomer*, 10(3-4), 42–43.
- Suggs, R. M., Cooke, W. J., Suggs, R. J. et al. (2008). The nasa lunar impact monitoring program. *Advances in Meteoroid and Meteor Science*, (pp. 293–298).
- Topputo, F., Merisio, G., Franzese, V. et al. (2023). Meteoroids detection with the lumio lunar cubesat. *Icarus*, 389, 115213.
- Vaniman, D., Reedy, R., Heiken, G. et al. (1991). The lunar environment. *The lunar Sourcebook, CUP*, (pp. 27–60).
- Virtanen, P., Gommers, R., Oliphant, T. E. et al. (2020). Scipy 1.0: fundamental algorithms for scientific computing in python. *Nature methods*, 17(3), 261–272.
- Xilouris, E., Bonanos, A., Bellas-Velidis, I. et al. (2018). Neliota: the wide-field, high-cadence, lunar monitoring system at the prime focus of the kryoneri telescope. *Astronomy & Astrophysics*, 619, A141.

- Yanagisawa, M., Ikegami, H., Ishida, M. et al. (2008). Lunar impact flashes by geminid meteoroids in 2007. *Meteoritics and Planetary Science Supplement*, 43, 5169.
- Yanagisawa, M., & Kisaichi, N. (2002). Lightcurves of 1999 leonid impact flashes on the moon. *Icarus*, 159(1), 31–38.
- Yanagisawa, M., Ohnishi, K., Takamura, Y. et al. (2006). The first confirmed perseid lunar impact flash. *Icarus*, 182(2), 489–495.